Composites

CrossMark

Flexible electrospun MWCNTs/Ag$_3$PO$_4$/PAN ternary composite fiber membranes with enhanced photocatalytic activity and stability under visible-light irradiation

Xiao-Qiong Wu[1,2] (ID), Jiang-Shan Shen[3] (ID), Fei Zhao[1] (ID), Zai-Dong Shao[1] (ID), Lu-Bin Zhong[1] (ID), and Yu-Ming Zheng[1,*] (ID)

[1] CAS Key Laboratory of Urban Pollutant Conversion, Institute of Urban Environment, Chinese Academy of Sciences, Xiamen 361021, China
[2] University of Chinese Academy of Sciences, Beijing 100049, China
[3] College of Materials Science and Engineering, Huaqiao University, Xiamen 361021, China

ABSTRACT

Semiconductor photocatalysis is a promising technology for removing contaminants from water. Particularly, visible-light photocatalysis has attracted much attention because of its potential to utilize solar energy. However, nano-sized visible-light-driven photocatalysts easily aggregate during water treatment. Besides, it is difficult to recycle them from treated systems. Therefore, it is of great importance to develop visible-light-responsive immobilized photocatalysts with high activity. In this work, MWCNTs/Ag$_3$PO$_4$/polyacrylonitrile (PAN) ternary composite fiber membranes (TCFMs) with good photocatalytic performance were fabricated by electrospinning technique combined with in situ Ag$_3$PO$_4$ forming reaction. Due to the addition of MWCNTs, the band gap of MWCNTs/Ag$_3$PO$_4$/PAN TCFMs became narrower than that of Ag$_3$PO$_4$/PAN binary composite fiber membranes (BCFMs), which made MWCNTs/Ag$_3$PO$_4$/PAN TCFMs be able to use light at longer wavelengths. Compared with Ag$_3$PO$_4$/PAN BCFMs, the as-prepared MWCNTs/Ag$_3$PO$_4$/PAN TCFMs showed enhanced photocatalytic activity and stability for degrading rhodamine B (RhB) in batch processing systems, which mainly ascribed to fast electron transfer from Ag$_3$PO$_4$ to MWCNTs and the resulting high electron–hole (e$^-$–h$^+$) separation efficiency. Radical trapping experiments revealed that holes (h$^+$) and superoxide radicals ($\cdot$O$_2^-$) played primary roles in RhB degradation. In addition, the flexible MWCNTs/Ag$_3$PO$_4$/PAN TCFMs also showed potential practical application in the continuous wastewater treatment by a suitable photocatalytic membrane reactor. This work provides a facile approach to prepare flexible supported photocatalytic membrane with visible-light response, high activity and good stability.

Address correspondence to E-mail: ymzheng@iue.ac.cn

🙋 Springer

Introduction

Combination of solar energy and nanomaterial has been considered as one of the most promising technologies, which can overcome the issues of energy crisis and environmental pollution [1–3]. In particular, due to its potential application in removing environmental pollutants by using solar energy, semiconductor photocatalysis has received considerable attention [4]. In the process of photocatalysis, photogenerated electrons (e^-) and holes (h^+) can migrate to the surface of semiconductors and then react with the adsorbed species like water and oxygen to form radicals; these holes and/or radicals with strong oxidation can eventually decompose contaminants into harmless CO_2 and H_2O. Traditional photocatalysts, like TiO_2 and ZnO, cannot make use of visible light (400–700 nm) which accounts for 43% of the natural sunlight due to their wide band gaps (ca. 3.2 eV for both) [5–7]. Therefore, it is significant to develop visible-light-sensitive photocatalysts with high activity for practical application. Ag_3PO_4 is regarded as one of promising photofunctional materials with visible-light response for waste water treatment and water splitting [8]. Yi et al. has reported that Ag_3PO_4 has a direct transition of 2.43 eV and an indirect band gap of 2.36 eV. Thereby, it can use solar energy with the wavelength shorter than ca. 530 nm to degrade organic pollutants. It was also revealed that Ag_3PO_4 could achieve an extremely high apparent quantum yield (> 80%) of O_2 evolution at wavelengths less than ca. 480 nm using $AgNO_3$ as sacrificial reagent. The apparent quantum yield was significantly higher than that of other reported visible-light-driven photocatalysts, indicating very weak recombination of photoexcited electrons and holes within Ag_3PO_4 [9]. However, Ag_3PO_4 is slightly soluble in aqueous solution and is easily corroded by generated e^- to form Ag^0 nanoparticles (NPs) under light irradiation [10, 11]. The photocorrosion of Ag_3PO_4 results from its energy band structure as the conduction band energy of Ag_3PO_4 is much more positive than H_2O/H_2 potential yet more negative than Ag/Ag^+ potential [12].

The strategies that can improve the stability of Ag_3PO_4 include metal deposition [11, 13, 14], constructing heterostructure with other semiconductors [10, 15–20] and combining with carbon materials [7, 21–26]. In these systems, photogenerated e^- of Ag_3PO_4 could be transferred to other components,

slowing not only photocorrosion but also the recombination of e^- and h^+, resulting in enhanced photocatalytic stability and activity. Among these systems, carbon-based Ag_3PO_4 composites get more attention because carbon materials such as graphene (GR) and multi-wall carbon nanotubes (MWCNTs) possess unique properties such as large specific surface area, excellent electrical conductivity, great electronic mobility and stability [15]. By using the calculation of density functional theory, Xu et al. have investigated the mechanism of the enhanced visible-light photocatalytic performance and the stability of Ag_3PO_4/GR composite [21]. The large built-in potential formed at the interface and the narrowed band gap induced by interactions between GR and Ag_3PO_4 (100) can facilitate electrons transferring from Ag_3PO_4 into GR in the ground electronic state, thus enhancing the stability and activity of the Ag_3PO_4 (100)/GR composite [21].

Facile operation and easy recovery are also crucial to the practical use of Ag_3PO_4. In general, tedious post-separation processes are employed to recover Ag_3PO_4 particles from the treated liquid. However, Ag_3PO_4 particles have a strong tendency of agglomeration during the water treatment process, and such agglomeration would severely affect their photocatalytic activity, reusability and service life. Some efforts have been devoted to overcome these problems. By immobilizing Ag_3PO_4 particles on supports such as exfoliated bentonite [27], magnetic Fe_3O_4 [28, 29], and attapulgite [30], aggregation can be effectively avoided and it could be much easier for post-separation. However, these composites were in their powder forms, which would limit their practical use in the continuous water treatment. Electrospun fiber membranes (EFMs) produced by electrospinning are monolithic materials, which can be easily recycled from a liquid medium. Polyacrylonitrile (PAN) EFMs are widely used as the support for catalysts due to their low cost and high tensile strength. PAN-based Ag_3PO_4 composite EFMs have been first developed by Yu et al., which exhibited excellent photocatalytic activities for the degradation of organic contaminants under visible-light irradiation [31, 32]. Recently, Panthi et al. reported Ag_3PO_4/PAN composite EFMs with enhanced photocatalytic and antimicrobial activities prepared by surface oximation, in which amidoxime groups were acted as anchoring sites for Ag^+ ions by coordination bonding [33]. However, to our best knowledge, employing

carbon materials to further improve the stability and activity of PAN-based Ag_3PO_4 composite EFMs has not been studied yet.

In this work, we report the fabrication of flexible MWCNTs/Ag_3PO_4/PAN ternary composite fiber membranes (TCFMs) via facile electrospinning and in situ Ag_3PO_4 forming reaction (Fig. 1). MWCNTs were chosen as the electron conductors aiming to enhance photocatalytic activity and stability of Ag_3PO_4 under visible-light irradiation. The as-prepared MWCNTs/Ag_3PO_4/PAN TCFMs were systematically characterized and their photocatalytic activity and stability under visible-light irradiation were evaluated by degrading a model contaminant—rhodamine B (RhB) in batch processing systems. Compared with Ag_3PO_4/PAN binary composite fiber membranes (BCFMs), the as-prepared MWCNTs/Ag_3PO_4/PAN TCFMs showed much higher photocatalytic activity and stability. Based on the identified reactive species, a possible reaction mechanism for photocatalytic degradation of RhB by MWCNTs/Ag_3PO_4/PAN TCFMs under visible-light irradiation was proposed. In addition, the feasibility of continuously degrading RhB by flexible MWCNTs-1%/Ag_3PO_4/PAN TCFMs under visible-light irradiation was checked using a homemade photocatalytic membrane reactor.

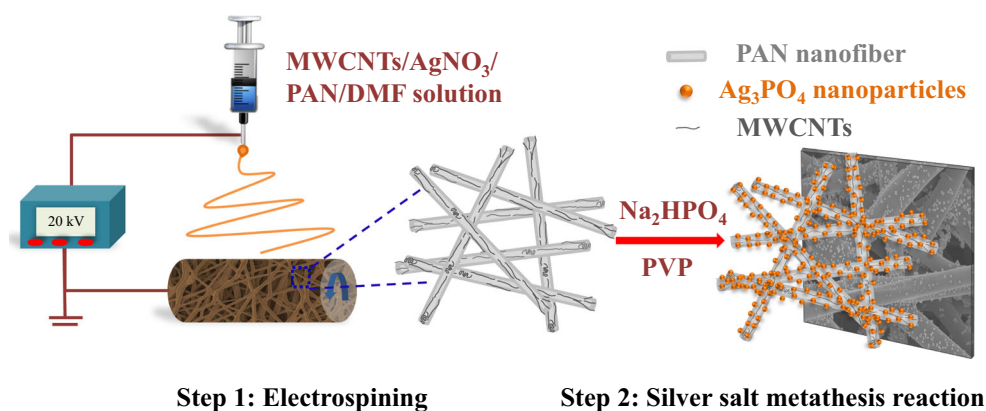## Materials and methods

Materials

MWCNTs (purity > 95 wt%, OD = 30–50 nm, length = 0.5–2 μm) were obtained from Chengdu Organic Chemicals Co., Ltd., Chinese Academy of Sciences. PAN (M_w = 90000 g/mol) was purchased from Kunshan Hongyu Plastics Co., Ltd. (Suzhou, China). N, N-dimethylformamide (DMF), Na_2HPO_4, formic acid (FA) and isopropyl alcohol (IPA) were commercially available from Sinopharm Chemical Reagent Co., Ltd. (Shanghai, China). PVP and p-benzoquinone (BQ) were purchased from Aladdin Industrial Co. (Shanghai, China). $AgNO_3$ was purchased from Shanghai Chemical Reagent Co., China and RhB was received from Sangon Biotech (Shanghai) Co., Ltd. The ultrapure water (18.2 Ω) used in throughout experiments was produced by a Milli-Q system (Millipore, Massachusetts). All chemicals used in this work were of analytical grade and used without further purification.

Fabrication of MWCNTs/Ag_3PO_4/PAN TCFMs

The MWCNTs/Ag_3PO_4/PAN TCFMs were synthesized by combining electrospinning with in situ Ag_3PO_4 forming reaction, basing on a modified method [32]. Typically, 3.6 g of PAN powder was dissolved in 26.4 g of DMF, and vigorously stirred at room temperature for 2 h to obtain a homogeneous solution. Then, different amounts of MWCNTs (0.018, 0.036, 0.108, 0.18, 0.288 and 0.36 g) were dispersed in the above solution to obtain MWCNTs-x%/PAN homogeneous black solution (x refers to 0.5, 1, 3, 5, 8 and 10 accordingly). The resulting mixture was then stirred in a water bath at 60 °C for another 6 h. After that, 1.8 g of $AgNO_3$ was added into the mixed solution, and stirred for 2 h at room temperature to completely dissolve $AgNO_3$. Subsequently, the as-prepared spinning solution was transferred to a 20 mL syringe with a 19-gauge metal needle. The feeding rate was set as 0.8–1.5 mL h^{-1} according to different systems, and the tip-to-collector distance

Figure 1 Schematic diagram of the preparation of electrospun MWCNTs/Ag_3PO_4/PAN ternary composite fiber membranes (TCFMs).

MWCNTs/$AgNO_3$/PAN/DMF solution

20 kV

Na$_2$HPO$_4$

PVP

PAN nanofiber

Ag_3PO_4 nanoparticles

MWCNTs

Step 1: Electrospining

Step 2: Silver salt metathesis reaction

was fixed to 15 cm. The electrospinning voltage was set to 25–40 kV, and the TCFMs were collected by an aluminum foil. The collected TCFMs were then laminated by a paper laminator (No. 3893, Deli, China) to obtain nascent MWCNTs-$x\%$/AgNO$_3$/PAN TCFMs.

In order to obtain MWCNTs-$x\%$/Ag$_3$PO$_4$/PAN TCFMs, nascent MWCNTs-$x\%$/AgNO$_3$/PAN TCFMs were immersed into a 0.4 M Na$_2$HPO$_4$ aqueous solution containing 0.1 M PVP at room temperature for 5 min. The obtained MWCNTs-$x\%$/Ag$_3$PO$_4$/PAN TCFMs were washed by ultrapure water several times to remove the residual reactants and PVP. After drying at 60 °C for 2 h, the as-prepared TCFMs were stored in zip-lock bags for further experiments. The fabrication process of Ag$_3$PO$_4$/PAN BCFMs (abbreviated as MWCNTs-0%/Ag$_3$PO$_4$/PAN in figures and tables) was similar to that of MWCNTs/Ag$_3$PO$_4$/PAN TCFMs, except for adding MWCNTs.

Characterization of MWCNTs/Ag$_3$PO$_4$/PAN TCFMs

X-ray diffraction (XRD) experiments were performed on a Panalytical X'pert PRO diffractometer equipped with Cu Kα radiation (λ = 1.5418 Å), and the XRD patterns were recorded from 10° to 90° with a scan step time of 13.77 s. The morphologies of the as-prepared TCFMs were probed by employing a field emission scanning electron microscopy (FESEM) (S-4800, HITACHI, Japan) operating at an accelerating voltage of 5 kV. Transmission electron microscopy (TEM) observations were done on a HITACHI H-7650 system. UV–Vis absorption spectra were recorded on a Thermo Evolution 300 absorption spectrophotometer with a 1-cm quartz cell. IR experiments were done on a Fourier transform infrared spectroscopy (FTIR, iS10, Thermo, USA) with a transmission mode. The Raman measurements were performed on a confocal microscope Raman spectrometer (LabRAM Aramis, France). UV–Vis diffuse reflection spectra (DRS) were measured by a UV–Vis-NIR spectrophotometer (Shimadzu, UV-3600, Japan). The chemical composition was probed by an X-ray photoelectron spectroscopy (XPS) (ESCALAB250, Thermo Fisher Inc., USA).

Photocatalytic experiments

Photocatalytic experiments were tested in batch systems. The photocatalytic performances of the MWCNTs/Ag$_3$PO$_4$/PAN TCFMs and Ag$_3$PO$_4$/PAN BCFMs for degrading RhB were evaluated by using a 300 W Xe arc lamp (HSX-F300, NBET of S&T co., Ltd., Beijing) with a 420-nm cutoff filter as the light source at ambient temperature. 0.2 g of the MWCNTs/Ag$_3$PO$_4$/PAN TCFMs or Ag$_3$PO$_4$/PAN BCFMs was added in a Pyrex photocatalytic reactor containing 100 mL of RhB solution (8.0 mg L^{-1}). Before irradiation, the solution was magnetically stirred for 40 min in the dark to reach the adsorption–desorption equilibrium. After irradiation, 1.5 mL of the solution was pipetted at certain time interval and checked by a UV–Vis absorption spectrometer (Thermo Evolution 300, USA). The absorbance at wavelength of 552 nm was recorded. The removal efficiency (R) of RhB was determined according to the following equation:

$$R = (1 - A/A_0) \times 100\% \tag{1}$$

where A is the absorbance at 552 nm of RhB solution at various light irradiation time t, A_0 is the absorbance at 552 nm of RhB solution when reaching the adsorption–desorption equilibrium (before light irradiation). For stability experiments, after the reaction was ended, the samples were recycled and washed by ultrapure water several times, and then the samples were dried at 60 °C for 24 h for next cycle. IPA (100 μL), BQ (5 mg), and FA (100 μL) acting as the scavengers of ˙OH, ˙O$_2^-$, and h$^+$ were added into the photocatalytic systems to conduct radical trapping experiments.

Photocatalytic experiments were also tested in the continuous treatment systems. 200-mL simulated waste water containing various RhB concentrations (1, 2, 4, 8 mg L^{-1}) was driven by a peristaltic pump (BT100-1L, Longer, China) to flow into a homemade photocatalytic membrane reactor. The as-prepared MWCNTs-1%/Ag$_3$PO$_4$/PAN TCFMs with diameter of 7 cm were supported by an acrylic perforated plate and non-woven fabrics. All these materials were fixed between upper and bottom sections of the reactor by using a seal cushion and 6 bolts. The 300-W Xe arc lamp with a 420-nm cutoff filter was put ca. 5 cm from the top of the reactor. The treated water permeated through the membranes and flowed back into the container for circulation. 3 mL of the liquid was sampled from the container at given time

intervals and tested immediately by a UV–Vis absorption spectrometer (Thermo Evolution 300, USA). The flow rates were set to 10, 30 and 50 mL min^{-1} and the initial concentrations were set to 1, 2, 4 and 8 mg L^{-1} to evaluate the effect of flow rate and initial concentration in this system.

Results and discussion

Characterization of the MWCNTs/Ag$_3$PO$_4$/PAN TCFMs

The morphologies of the as-prepared MWCNTs/AgNO$_3$/PAN TCFMs and MWCNT/Ag$_3$PO$_4$/PAN TCFMs were investigated by SEM (taking $x = 1$ as an example). Before in situ forming Ag$_3$PO$_4$ NPs, the MWCNTs-1%/AgNO$_3$/PAN TCFMs possessed relatively uniform fibers with an average diameter of 882 ± 9 nm (Fig. 2a and Fig. S1a). The fibers with smooth surface were randomly interwoven together forming 3-dimensional (3D) open structure (Fig. 2b). After the reaction between AgNO$_3$ and Na$_2$HPO$_4$ in the presence of PVP, the average fiber diameters of MWCNTs-1%/Ag$_3$PO$_4$/PAN TCFMs became larger (1156 ± 15 nm) (Fig. S1b) and the surface of the fibers turned to be rougher (Fig. 2c). The in situ formed tetrahedrons Ag$_3$PO$_4$ NPs were uniformly immobilized on the surface of fibers (Fig. 2d and the inset) with the average size of 107 ± 2 nm (Fig. S1c). The formation of Ag$_3$PO$_4$ NPs on the surface of fibers can also be indicated by the color change from gray (inset in Fig. 2a) to olive green (inset in Fig. 2c). The morphology of the Ag$_3$PO$_4$/PAN BCFMs was similar to those of MWCNTs-1%/Ag$_3$PO$_4$/PAN TCFMs (Fig. S2), which indicated that introducing MWCNTs hardly affect in situ forming Ag$_3$PO$_4$ NPs.

TEM observations further confirmed the presence of uniform Ag$_3$PO$_4$ NPs layers on the surface of MWCNTs/PAN fibers and the distribution of MWCNTs within fibers (Fig. 3). MWCNTs can be either totally wrapped within the fibers intertwining together or partially embedded in the fibers, as shown by the red arrows in Fig. 3b, c. Such distribution of MWCNTs was considered to be beneficial to the photocatalytic performance of the in situ formed Ag$_3$PO$_4$ NPs on the surface of fibers [24].

XRD experiments revealed that all the diffraction peaks of the MWCNTs/Ag$_3$PO$_4$/PAN TCFMs with different contents of MWCNTs and the Ag$_3$PO$_4$/ PAN BCFMs could be well indexed as the body-centered cubic Ag$_3$PO$_4$ (JCPDS card No. 01-070-0702) (Fig. 4). The sharp and intense diffraction peaks were indicative of the highly crystalline nature of the in situ formed Ag$_3$PO$_4$ NPs. For all the samples, the peaks corresponding to (010) plane of PAN became broader and shifted to ca. 2θ of 17.1°, while the peak of pristine PAN NFs centered at 2θ of 16.7° (PDF No. 048-2119) (Fig. S3) [34]. Such shift was supportive of the existence of internal stress and imperfect crystal lattice within PAN fibers caused by the interaction between PAN and Ag$_3$PO$_4$ NPs [35]. The weak XRD peak located at ca. 26.1° of MWCNTs/Ag$_3$PO$_4$/PAN TCFMs can be assigned to (002) plane of MWCNTs (Fig. S3) [7]. The diffraction intensity of this peak generally increased with increasing MWCNTs content. These results supported that Ag$_3$PO$_4$ NPs and MWCNTs were successfully introduced into the PAN fibers.

The average size of Ag$_3$PO$_4$ NPs could be estimated according to the following Debye–Scherrer formula:

$$D = \mathrm{K}\lambda/\beta\cos\theta \tag{2}$$

in which D is the diameter of nanoparticles (nm), λ is the wavelength of the incident X-ray (Cu Kα = 0.154056 nm), K is the Scherrer constant (K = 0.89), β is full width at half-maximum (FWHM) of the (210) plane of Ag$_3$PO$_4$, and θ is the X-ray diffraction angle. The sizes of Ag$_3$PO$_4$ NPs in the TCFMs with different MWCNTs contents were calculated to be in the range of 75–110 nm, which is well agreed with the SEM observation. The results suggest that the content of MWCNTs could have slightly influence on the size of Ag$_3$PO$_4$.

XPS analysis was further performed to probe the chemical compositions of the MWCNTs-1%/Ag$_3$PO$_4$/PAN TCFMs (Fig. 5). A total scan spectrum in the binding energy range of 0–800 eV revealed that Ag, P, O, C and N elements coexist in the TCFMs (Fig. 5a). Two peaks positioned at 367.75 and 373.80 eV in high resolution spectrum of Ag 3d (Fig. 5b) can be assigned to the electron orbits of Ag 3d$_{5/2}$ and Ag 3d$_{3/2}$ of Ag$^+$, respectively [16]. The peak with binding energy at 133.08 eV can be ascribed to P 2p of PO$_4^{3-}$ (Fig. 5c). The C 1s XPS spectrum of the NFMs can be deconvoluted into three peaks located at 284.80, 286.15 and 288.30 eV (Fig. 5d), which were assigned to the carbons in C–C, –C≡N/ CH, and O–C=O/C–O (from co-monomers) groups
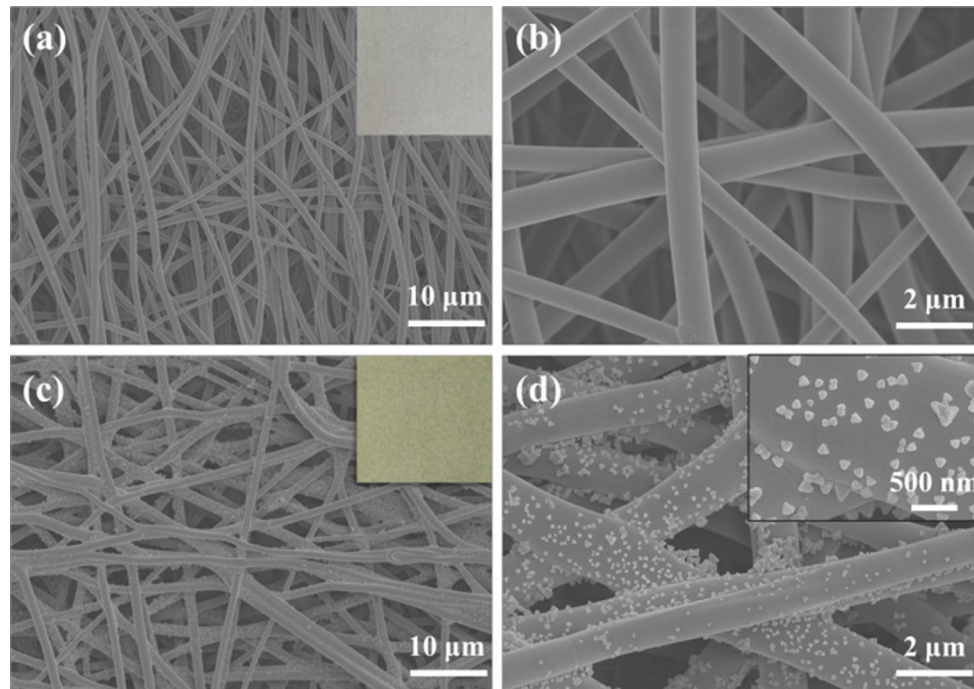
Figure 2 SEM images of MWCNTs-1%/AgNO$_3$/PAN TCFMs **a** and **b**; MWCNTs-1%/Ag$_3$PO$_4$/PAN TCFMs **c** and **d**. Insets in **a** and **c**: optical photographs of TCFMs; inset in **d**: magnified SEM image of Ag$_3$PO$_4$ NPs.
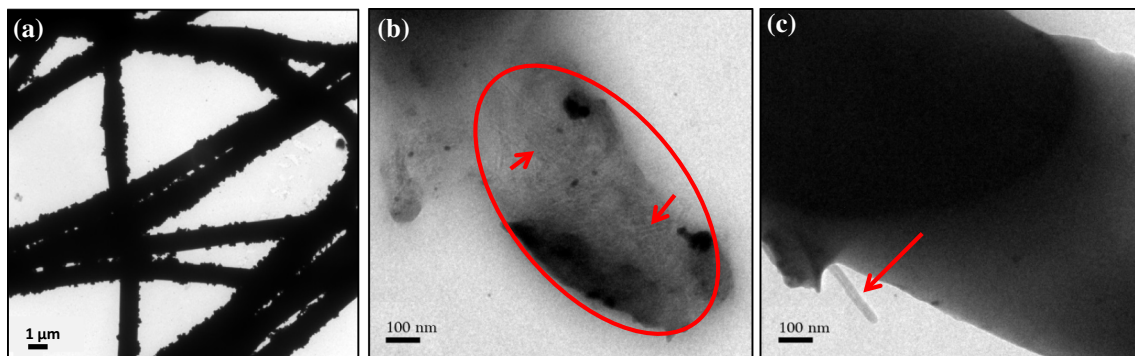

Figure 3 TEM images of **a** MWCNT-1%/Ag$_3$PO$_4$/PAN TCFMs; **b** MWCNTs intertwining together within cracked fibers; **c** MWCNTs being partly embedded within the fibers.

of PAN, respectively [36]. FTIR were carried out to further support the existence of –CN group, P–O stretching vibration, C–C band and aliphatic –CH$_2$– group vibrations in MWCNTs/Ag$_3$PO$_4$/PAN TCFMs with MWCNTs contents of 1, 3 and 5% (see details in Supporting Information, Fig. S4). These results can be substantially indicative of the successful fabrication of MWCNTs/Ag$_3$PO$_4$/PAN TCFMs.

UV–Vis DRS measurements were also carried out to investigate the optical properties and energy band structure of the Ag$_3$PO$_4$/PAN BCFMs and the MWCNTs/Ag$_3$PO$_4$/PAN TCFMs with different MWCNTs contents (Fig. 6). The light absorption intensity of MWCNTs/Ag$_3$PO$_4$/PAN TCFMs increased with increasing MWCNTs content and was higher than that of Ag$_3$PO$_4$/PAN BCFMs (Fig. 6a). The corresponding color of the MWCNTs/Ag$_3$PO$_4$/PAN TCFMs was also observed to change from yellow to olive green with increasing MWCNTs content. The band gaps of Ag$_3$PO$_4$/PAN BCFMs and MWCNTs/Ag$_3$PO$_4$/PAN TCFMs were calculated based on the corresponding UV–Vis DRS spectra by using the following formula (Eq. 3) [24]:

$$(Ahv)^2 = hv - E_g \qquad (3)$$

in which A is the absorbance, h is the Planck's constant, v is the frequency of the incident photon and E_g is the band gap. As shown in Fig. 6b, the band gap of Ag_3PO_4/PAN BCFMs could be determined to be 2.4 eV, which was very close to that of in previous report [9]. However, the band gaps of MWCNTs/Ag_3PO_4/PAN TCFMs with various MWCNTs contents were smaller than that of Ag_3PO_4/PAN BCFMs and decreased with increasing MWCNTs content
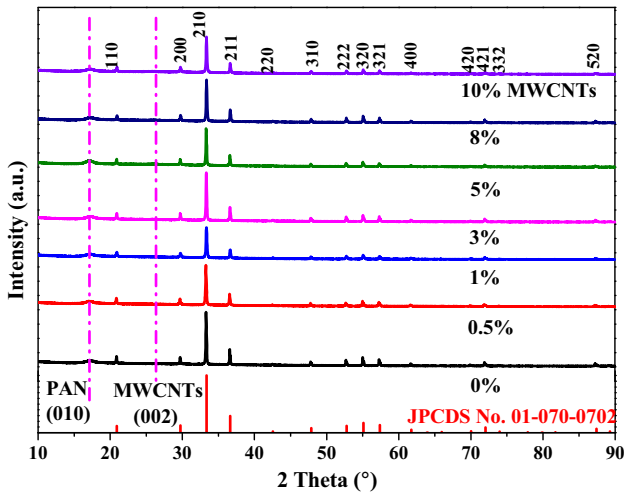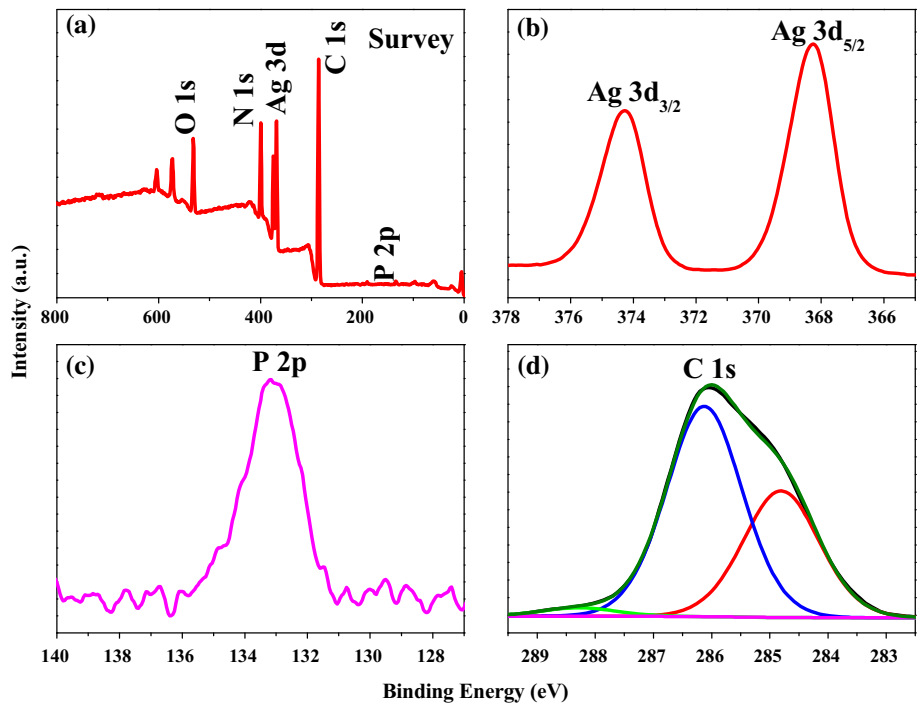

Figure 4 XRD patterns of MWCNTs/Ag_3PO_4/PAN TCFMs with different contents (0, 0.5, 1, 3, 5, 8 and 10%) of MWCNTs.

(Fig. 6b). These observations indicated that adding MWCNTs can narrow the band gap of Ag_3PO_4/PAN composite and this reduction was related to the amount of MWCNTs. The absorption edge could be calculated based on the empirical formula below:

$$\lambda_{max} = 1240/E_g \qquad (4)$$

in which λ_{max} is the absorption edge. As the band gaps of all MWCNTs/Ag_3PO_4/PAN TCFMs were smaller than that of Ag_3PO_4/PAN BCFMs, the absorption edges shifted toward the longer wavelengths, thus to absorb much more visible light (listed in Table S1). The energy band structure of samples could be estimated according to the following empirical equations [19]:

$$E_{VB} = \chi - E_0 + 0.5E_g \qquad (5)$$

$$E_{CB} = E_{VB} - E_g \qquad (6)$$

in which E_{VB} is the valance band (VB); E_{CB} is the conduct band (CB); χ is the absolute electronegativity of the photocatalyst calculated by geometric mean of electronegativity of constituent atoms, which is defined as the arithmetic mean of the atomic electron affinity and the first ionization energy; E_0 is the energy of free electron on the hydrogen scale (ca. 4.5 eV vs. normal hydrogen electrode (NHE)). The value of χ for Ag_3PO_4 is 6.16 eV versus NHE [10]; therefore, E_{VB} of Ag_3PO_4/PAN BCFMs and

Figure 5 XPS spectra of MWCNTs-1%/Ag_3PO_4/PAN TCFMs: **a** the total survey scan, **b** Ag 3d, **c** P 2p and **d** C 1s.
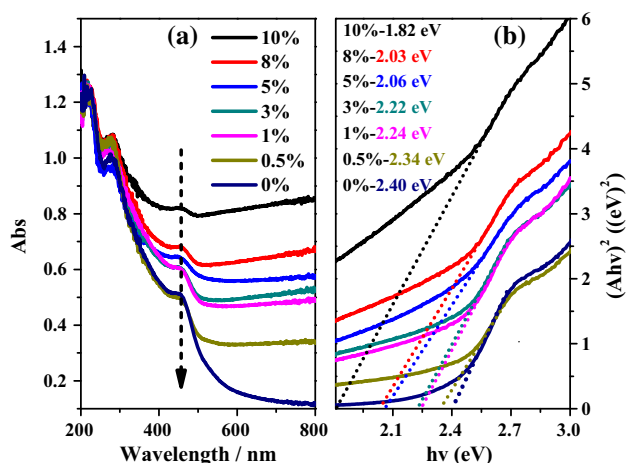
Figure 6 **a** UV–Vis DRS and **b** the plots of $(Ahv)^2$ versus energy (hv) based on the DRS spectra of MWCNTs/Ag$_3$PO$_4$/PAN TCFMs with different content of MWCNTs.

Figure 7 Raman spectra of the MWCNTs and MWCNTs-1%/Ag$_3$PO$_4$/PAN TCFMs.

MWCNTs-1%/Ag$_3$PO$_4$/PAN TCFMs could be calculated to be 2.86 and 2.78 eV versus NHE, and the corresponding E_{CB} could also be calculated to be 0.46 and 0.54 eV versus NHE, respectively. These shifts of both CB minimum (CBM) and VB maximum (VBM) can be contributed to the interfacial interaction between MWCNTs and Ag$_3$PO$_4$ NPs, which may be similar to the interaction between GR and Ag$_3$PO$_4$ in GR/Ag$_3$PO$_4$ nanocomposite reported by Xu et al. [21].

The interfacial charge transfer between MWCNTs and Ag$_3$PO$_4$ NPs was probed by Raman spectroscopy. For MWCNTs powder, two bands at ca. 1345 and 1576 cm^{-1} were observed (Fig. 7), which were the typical Raman features referring to D-band and G-band of MWCNTs [37]. For MWCNTs-1%/Ag$_3$PO$_4$/PAN TCFMs, however, the G-band shifted by 9 cm^{-1} to a lower frequency at 1567 cm^{-1} (Fig. 7). Such shift is considered to be caused by the interfacial charge transfer between carbon materials and the hybridized components [38]. In general, G-band of MWCNTs shifts to high frequency when MWCNTs are hybridized with an electron acceptor component, yet it shifts to a low frequency when MWCNTs are hybridized with an electron donor component [39]. Therefore, it can be concluded that electrons can transfer from Ag$_3$PO$_4$ to MWCNTs in MWCNTs/Ag$_3$PO$_4$/PAN TCFMs under light irradiation, which would be beneficial for their photocatalytic activity and stability.
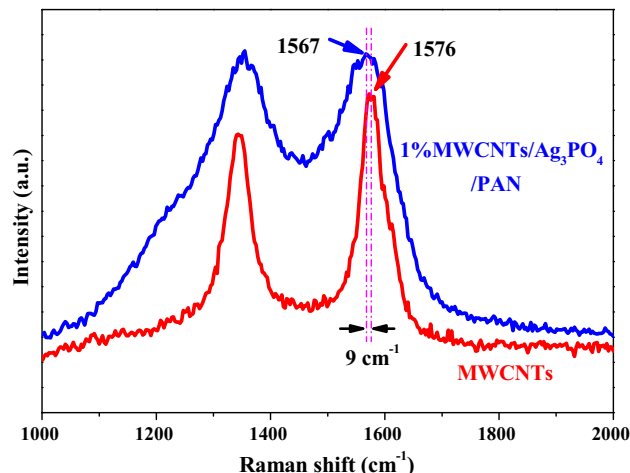
Photocatalytic activity and stability of the MWCNTs/Ag$_3$PO$_4$/PAN TCFMs and the Ag$_3$PO$_4$/PAN BCFMs in batch systems

The photocatalytic activity of the as-prepared MWCNTs/Ag$_3$PO$_4$/PAN TCFMs and Ag$_3$PO$_4$/PAN BCFMs were investigated employing RhB as a model contaminant in batch systems under visible-light irradiation ($\lambda \geq 420$ nm). Without the photocatalyst, RhB concentration was found to be hardly changed under visible-light irradiation (line "Blank" in Fig. 8a), indicating that self-photolysis of RhB can be neglected under this experimental condition. When the photocatalysts were added into the systems, adsorption–desorption equilibrium of RhB between the samples and aqueous solution could be reached within 40 min in the dark ("light off" stage in Fig. 8a). The removal efficiencies by adsorption were less than 8% for all the used photocatalysts and there was little difference among them. For the system with MWCNTs-1%/Ag$_3$PO$_4$/PAN TCFMs, after irradiation, the color of RhB solution was found to be gradually changed from its original rose pink to colorless and the corresponding absorption peak at 552 nm drastically decreased with increasing time and eventually disappeared when the reaction time was about 80 min (Fig. S5).

To further compare the photocatalytic activity of the MWCNTs/Ag$_3$PO$_4$/PAN TCFMs and Ag$_3$PO$_4$/PAN BCFMs, pseudo-first-order kinetics model was employed to evaluate the apparent rate constants of
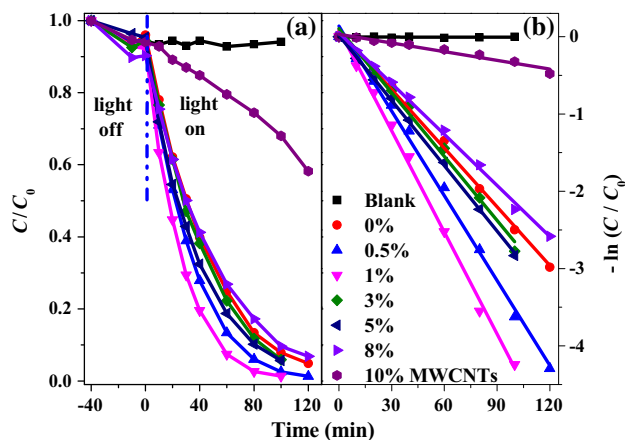
Figure 8 **a** Photocatalytic activities of MWCNTs/Ag$_3$PO$_4$/PAN TCFMs with different contents of MWCNTs and Ag$_3$PO$_4$/PAN BCFMs for the degradation of RhB solution under visible-light irradiation ($\lambda \geq 420$ nm) at room temperature, and **b** the corresponding kinetic linear simulation curves. Experiment conditions: [RhB] = 8 mg L^{-1}; [photocatalysts] = 2 g L^{-1}.

Table 1 Pseudo-first-order rate constants and regression coefficients of photocatalytic RhB degradation under visible-light illumination

No.	Photocatalyst MWCNTs-x%/Ag$_3$PO$_4$/PAN	k_{app} (min^{-1})	R^2
1	0	0.025	0.997
2	0.5	0.037	0.996
3	1	0.044	0.996
4	3	0.034	0.991
5	5	0.028	0.999
6	8	0.022	0.997
7	10	0.004	0.959

these photocatalytic reactions according to the following equation:

$$-\ln(C/C_0) = k_{app}t \tag{7}$$

in which C is the RhB concentration at time t, C_0 is the initial concentration of RhB, and k_{app} is the apparent reaction rate constant. The linear relationship between $\ln(C/C_0)$ and t reveals that all the degradation processes of the employed photocatalysts can be fitted well to follow pseudo-first-order kinetics (Fig. 8b). The estimated apparent degradation rate constants of RhB degradation in the presence of the MWCNTs/Ag$_3$PO$_4$/PAN TCFMs with different contents of MWCNTs and Ag$_3$PO$_4$/PAN BCFMs are summarized in Table 1. The results showed that adding a certain amount of MWCNTs (x = 0.5–5%) could enhance the photocatalytic activity of Ag$_3$PO$_4$/PAN BCFMs. MWCNTs-1%/Ag$_3$PO$_4$/PAN TCFMs were found to possess the highest photocatalytic degradation efficiency with the calculated k_{app} of 0.044 min^{-1}, which was ca. 1.8-fold higher than that of Ag$_3$PO$_4$/PAN BCFMs (0.025 min^{-1}). However, when the content of MWCNTs was increased to 8 and 10%, the photocatalytic activity was even lower than that of Ag$_3$PO$_4$/PAN BCFMs (Fig. 8a, b). This might be ascribed to good light-absorbing property of MWCNTs as the redundant MWCNTs on the surface of fibers could compete with Ag$_3$PO$_4$ NPs to absorb the incident light. This could severely decrease the light absorbed by Ag$_3$PO$_4$ NPs, which would lessen

the generation of e$^-$ and h$^+$, resulting in worse performance [40].

Stability of photocatalysts is considered to be an important factor for their practical applications. In order to investigate the photocatalytic stability of the MWCNTs-1%/Ag$_3$PO$_4$/PAN TCFMs and Ag$_3$PO$_4$/PAN BCFMs, recycle experiments of RhB degradation by them were conducted. After three recycles, the removal efficiency of RhB by MWCNTs-1%/Ag$_3$PO$_4$/PAN TCFMs decreased less than 21% (Fig. 9), which is much lower than that of by Ag$_3$PO$_4$/PAN NFMs (ca. 45%). These results revealed that MWCNTs-1%/Ag$_3$PO$_4$/PAN TCFMs possess higher photocatalytic stability than that of Ag$_3$PO$_4$/PAN BCFMs. The slight decline of the activity may result from the reason that some Ag$_3$PO$_4$ NPs on the surface would fall off from the fibers. Modified method like grafting technique would be employed to further improve the bonding force between Ag$_3$PO$_4$ NPs and fibers. In addition, the antibacterial property and toxicity caused by those TCFMs will be investigated in our further study to evaluate the safety and environmental risks.

Photocatalytic degradation mechanisms

Radicals trapping experiments were conducted to explore the radical species being responsible for the photocatalytic degradation of RhB. During these experiments, IPA was used as the scavenger of ·OH, while BQ and FA were chosen as the scavengers of ·O$_2^-$ and h$^+$, respectively [18]. Figure 10 shows the comparison of photocatalytic activity of MWCNTs-1%/Ag$_3$PO$_4$/PAN TCFMs in the absence or presence of different scavengers. Introducing IPA could hardly
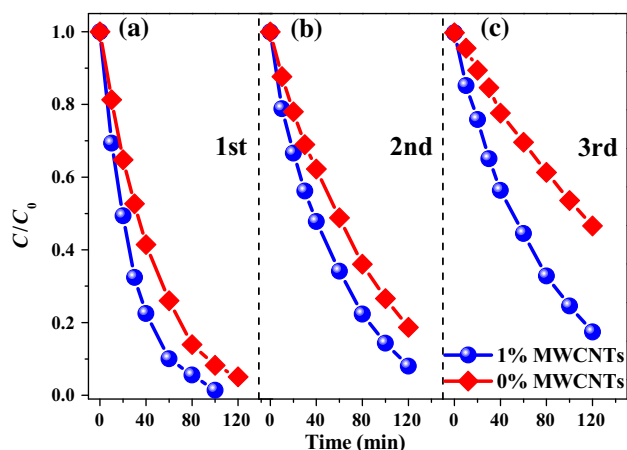
Figure 9 Comparison of photocatalytic efficiency of MWCNTs-1%/Ag$_3$PO$_4$/PAN TCFMs and Ag$_3$PO$_4$/PAN BCFMs of degrading RhB in the cycle of three times. Experiment conditions: [RhB] = 8 mg L^{-1}; [photocatalysts] = 2 g L^{-1}.

affect the photocatalytic degradation of RhB, revealing that $\cdot$OH was not the main oxidizing radicals in the degradation process. However, the photocatalytic activity could be significantly inhibited by BQ or FA, indicating that both $\cdot$O$_2^-$ and h$^+$ were responsible for RhB degradation.

On the basis of the above experiment results, a possible photocatalytic reaction mechanism is proposed (Fig. 11). Ag$_3$PO$_4$ NPs uniformly distributed on the surface of MWCNTs-1%/PAN fibers could be excited by visible light ($\lambda \leq 554$ nm) to generate e$^-$ in
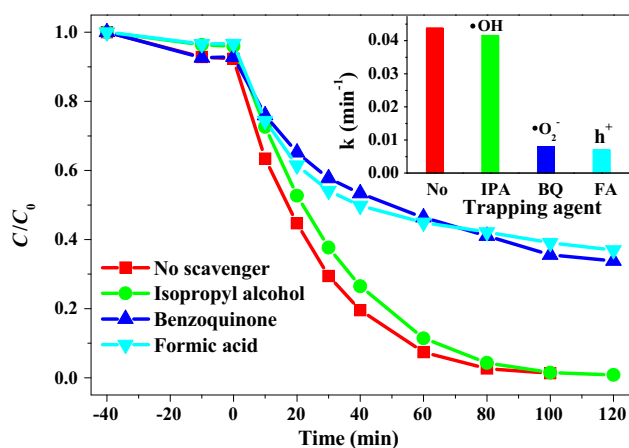
CB (0.54 eV) and h$^+$ in VB (2.78 eV). In Ag$_3$PO$_4$/PAN BCFMs system, the separated h$^+$ could directly oxidize RhB on the surface of Ag$_3$PO$_4$ NPs, while e$^-$ can be captured by Ag$_3$PO$_4$ to produce Ag^0, resulting in photocorrosion of Ag$_3$PO$_4$ NPs. However, in the presence of conductive MWCNTs, the excited e$^-$ can be transferred to MWCNTs and react with O$_2$ absorbed on the surface of photocatalyst to produce $\cdot$O$_2^-$. Both h$^+$ and $\cdot$O$_2^-$ with strong oxidation capability can effectively degrade RhB under visible-light irradiation. The efficient transfer of electrons from Ag$_3$PO$_4$ NPs to MWCNTs can offer the following two benefits: (1) the recombination of e$^-$ and h$^+$ can be effectively inhibited, increasing the separation efficiency of e$^-$ and h$^+$, thus to enhance the photocatalytic activity; (2) electrons can be away from Ag$_3$PO$_4$ NPs, reducing the photocorrosion of Ag$_3$PO$_4$ NPs, thereby to improve the photocatalytic stability. Furthermore, MWCNTs likely offer more active adsorption and reaction sites.

Photocatalytic performance in continuous treatment system

Considering the enhanced photocatalytic performance and flexibility (Fig. S6), the as-prepared MWCNTs-1%/Ag$_3$PO$_4$/PAN TCFMs are expected to have practical application in continuous water treatment. Therefore, the feasibility of continuously degrading RhB in the presence of MWCNTs-1%/Ag$_3$PO$_4$/PAN TCFMs under visible-light irradiation
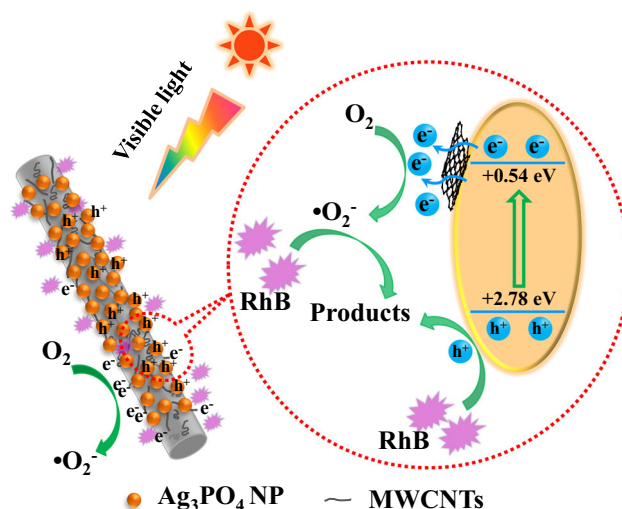

Figure 10 The evolution of photocatalytic activity of MWCNTs-1%/Ag$_3$PO$_4$/PAN TCFMs of degrading RhB in the presence of different trapping agents. Inset is corresponding pseudo-first-order rate constants. Experiment conditions: [RhB] = 8 mg L^{-1}; [photocatalysts] = 2 g L^{-1}; [IPA] = 0.79 g L^{-1}; [BQ] = 0.05 g L^{-1}; [FA] = 1.22 g L^{-1}.

Figure 11 Proposed reaction mechanism for photocatalytic degradation of RhB using MWCNTs-1%/Ag$_3$PO$_4$/PAN TCFMs under visible-light irradiation ($\lambda \geq 420$ nm).

was evaluated by a homemade photocatalytic membrane reactor (Fig. 12a). RhB solution flowed in from the top and then permeated through the membrane to flow out from the bottom outlet. The solution was repeatedly treated and 3 mL of the solution was taken out at given time intervals for detecting RhB concentration. The removal rates were found to be affected by flow rate and the initial concentration of RhB solution.

As shown in Fig. 12b, the removal rates of RhB were 89.4, 88.3 and 96.9% when the flow rates were 10, 30 and 50 mL min^{-1}, respectively (initial concentration was 2 mg L^{-1}). Figure 12c shows the photocatalytic degradation of RhB solution with different initial concentrations (1, 2, 4 and 8 mg L^{-1}) in MWCNTs-1%/Ag$_3$PO$_4$/PAN TCFMs system with flow rate of 30 mL/min. The removal rate was found to be enhanced when RhB concentration was increased from 1 to 4 mg L^{-1} (89.9, 89.4 and 96.4% for 1, 2 and 4 mg L^{-1}, respectively), but sharply decreased when the concentration was further increased to 8 mg L^{-1} (54.4%). These results indicated that it is feasible to employ MWCNTs/Ag$_3$PO$_4$/PAN TCFMs to continuously treat wastewater and the optimum treatment condition can be obtained by adjusting operating parameters. Moreover, it should be noted that no tedious or time-consuming separation process is needed in this membrane-based system, compared with other Ag$_3$PO$_4$ powder-based systems [22–25].

Conclusions

In conclusion, we have reported the fabrication of well-defined MWCNTs/Ag$_3$PO$_4$/PAN TCFMs by a facile method combining electrospinning technique and in situ Ag$_3$PO$_4$ forming reaction. The as-synthesized MWCNTs-1%/Ag$_3$PO$_4$/PAN TCFMs exhibited higher photocatalytic activity and stability in comparison with the Ag$_3$PO$_4$/PAN BCFMs under visible-light irradiation. The reasons include: (1) introducing MWCNTs could narrow the band gap of the Ag$_3$PO$_4$/PAN composite, resulting in that MWCNTs/Ag$_3$PO$_4$/PAN composite could utilize light with longer wavelengths; (2) adding MWCNTs could also lead to interfacial electron transfer from Ag$_3$PO$_4$ to MWCNTs, thus resulting in efficient separation of photogenerated e$^-$–h$^+$ pairs and less photocorrosion of Ag$_3$PO$_4$. Moreover, the as-prepared MWCNTs-1%/Ag$_3$PO$_4$/PAN TCFMs could be used as photocatalytic membranes in a suitable reactor for the continuous water treatment and these TCFMs could also be easily reused without any tedious or time-consuming separation process. This work provides an effective and simple approach to fabricate membrane-based composite photocatalysts with flexibil-
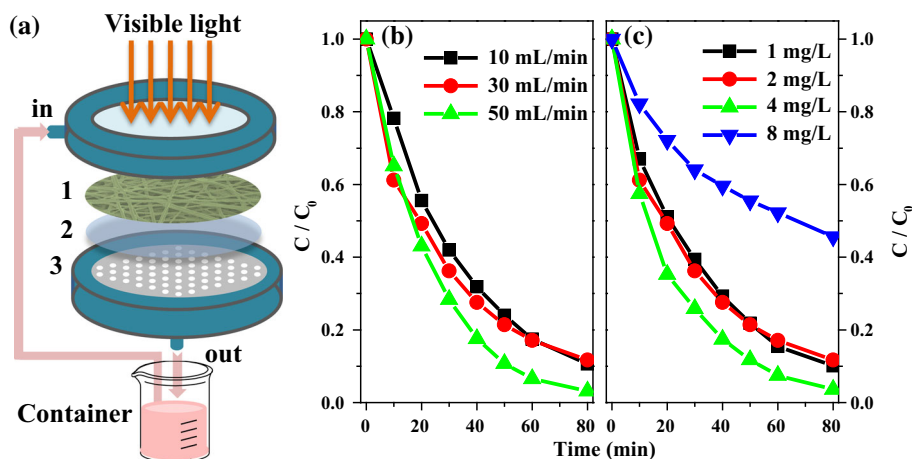

Figure 12 **a** Schematic illustration of the continuous treatment system: 1 represents MWCNTs-1%/Ag$_3$PO$_4$/PAN TCFMs; 2 represents non-woven fabrics; 3 represents acrylic perforated plate; **b** Treatment of 2 mg L^{-1} RhB solution in the continuous system in the presence of MWCNTs-1%/Ag$_3$PO$_4$/PAN TCFMs with different flow rates; and **c** photocatalytic degradation of RhB solution with different concentrations in MWCNTs-1%/Ag$_3$PO$_4$/PAN TCFMs system with 30 mL min^{-1} flow rate.

ity, visible-light response and high stability which are suitable for the continuous water treatment.

Acknowledgements

Electronic supplementary material: The online version of this article (https://doi.org/10.1007/s10853-018-2334-0) contains supplementary material, which is available to authorized users.

References

[1] Ong W-J, Tan L-L, Ng YH, Yong S-T, Chai S-P (2016) Graphitic carbon nitride (g-C_3N_4)-based photocatalysts for artificial photosynthesis and environmental remediation: are we a step closer to achieving sustainability? Chem Rev 116:7159–7329

[2] Mateo D, Esteve-Adell I, Albero J, Royo JFS, Primo A, Garcia H (2016) 111 oriented gold nanoplatelets on multilayer graphene as visible light photocatalyst for overall water splitting. Nat Commun 7:1–8

[3] Zhao X, Qu J, Liu H, Hu C (2007) Photoelectrocatalytic degradation of triazine-containing azo dyes at γ-Bi_2MoO_6 film electrode under visible light irradiation ($\lambda > 420$ Nm). Environ Sci Technol 41:6802–6807

[4] Li Y, Tang Z, Zhang J, Zhang Z (2016) Reduced graphene oxide three-dimensionally wrapped WO_3 hierarchical nanostructures as high-performance solar photocatalytic materials. Appl Catal A Gen 522:90–100

[5] Yao W, Zhang B, Huang C, Ma C, Song X, Xu Q (2012) Synthesis and characterization of high efficiency and stable Ag_3PO_4/TiO_2 visible light photocatalyst for the degradation of methylene blue and rhodamine B solutions. J Mater Chem 22:4050–4055

[6] Lee KM, Lai CW, Ngai KS, Juan JC (2016) Recent developments of zinc oxide based photocatalyst in water treatment technology: a review. Water Res 88:428–448

[7] Liu B, Li Z, Xu S, Han D, Lu D (2014) Enhanced visible-light photocatalytic activities of $Ag_3PO_4/MWCNT$ nanocomposites fabricated by facile in situ precipitation method. J Alloys Compd 596:19–24

[8] Martin DJ, Liu G, Moniz SJ, Bi Y, Beale AM, Ye J, Tang J (2015) Efficient visible driven photocatalyst, silver phosphate: performance, understanding and perspective. Chem Soc Rev 44:7808–7828

[9] Yi Z, Ye J, Kikugawa N, Kako T, Ouyang S, Stuart-Williams H, Yang H, Cao J, Luo W, Li Z, Liu Y, Withers RL (2010) An orthophosphate semiconductor with photooxidation properties under visible-light irradiation. Nat Mater 9:559–564

[10] Chen Z, Wang W, Zhang Z, Fang X (2013) High-efficiency visible-light-driven Ag_3PO_4/AgI photocatalysts: Z-scheme photocatalytic mechanism for their enhanced photocatalytic activity. J Phys Chem C 117:19346–19352

[11] Teng W, Li X, Zhao Q, Chen G (2013) Fabrication of Ag/Ag_3PO_4/TiO_2 heterostructure photoelectrodes for efficient decomposition of 2-chlorophenol under visible light irradiation. J Mater Chem A 1:9060–9068

[12] Chen X, Dai Y, Wang X (2015) Methods and mechanism for improvement of photocatalytic activity and stability of Ag_3PO_4: a review. J Alloys Compd 649:910–932

[13] Bi Y, Hu H, Ouyang S, Jiao Z, Lu G, Ye J (2012) Selective growth of Ag_3PO_4 submicro-cubes on Ag nanowires to fabricate necklace-like heterostructures for photocatalytic applications. J Mater Chem 22:14847–14850

[14] Hu H, Jiao Z, Wang T, Ye J, Lu G, Bi Y (2013) Enhanced photocatalytic activity of Ag/Ag_3PO_4 coaxial hetero-nanowires. J Mater Chem A 1:10612–10616

[15] Peng W-C, Wang X, Li X-Y (2014) The synergetic effect of MoS_2 and graphene on Ag_3PO_4 for its ultra-enhanced photocatalytic activity in phenol degradation under visible light. Nanoscale 6:8311–8317

[16] He Y, Zhang L, Teng B, Fan M (2015) New application of Z-scheme Ag_3PO_4/g-C_3N_4 composite in converting CO_2 to fuel. Environ Sci Technol 49:649–656

[17] Bu Y, Chen Z (2014) Role of polyaniline on the photocatalytic degradation and stability performance of the polyaniline/silver/silver phosphate composite under visible light. ACS Appl Mater Interfaces 6:17589–17598

[18] Tang C, Liu E, Wan J, Hu X, Fan J (2016) Co_3O_4 nanoparticles decorated Ag_3PO_4 tetrapods as an efficient visible-light-driven heterojunction photocatalyst. Appl Catal B Environ 181:707–715

[19] Katsumata H, Sakai T, Suzuki T, Kaneco S (2014) Highly efficient photocatalytic activity of g-C_3N_4/Ag_3PO_4 hybrid photocatalysts through Z-scheme photocatalytic mechanism under visible light. Ind Eng Chem Res 53:8018–8025

[20] You M, Pan J, Chi C, Wang B, Zhao W, Song C, Zheng Y, Li C (2018) The visible light hydrogen production of the Z-Scheme $Ag_3PO_4/Ag/g$-C_3N_4 nanosheets composites.

J Mater Sci 53:1978–1986. https://doi.org/10.1007/s10853-017-1612-6

[21] Xu L, Huang W-Q, Wang L-L, Huang G-F, Peng P (2014) Mechanism of superior visible-light photocatalytic cctivity and stability of hybrid Ag$_3$PO$_4$/graphene nanocomposite. J Phys Chem C 118:12972–12979

[22] Yang X, Cui H, Li Y, Qin J, Zhang R, Tang H (2013) Fabrication of Ag$_3$PO$_4$-graphene composites with highly efficient and stable visible light photocatalytic performance. ACS Catal 3:363–369

[23] Zhang H, Huang H, Ming H, Li H, Zhang L, Liu Y, Kang Z (2012) Carbon quantum dots/Ag$_3$PO$_4$ complex photocatalysts with enhanced photocatalytic activity and stability under visible light. J Mater Chem 22:10501–10506

[24] Xu H, Wang C, Song Y, Zhu J, Xu Y, Yan J, Song Y, Li H (2014) CNT/Ag$_3$PO$_4$ composites with highly enhanced visible light photocatalytic activity and stability. Chem Eng J 241:35–42

[25] Xiang Q, Lang D, Shen T, Liu F (2015) Graphene-modified nanosized Ag$_3$PO$_4$ photocatalysts for enhanced visible-light photocatalytic activity and stability. Appl Catal B Environ 162:196–203

[26] Ma J, Chen C, Yu F (2016) Self-regenerative and self-enhanced smart graphene/Ag$_3$PO$_4$ hydrogel adsorbent under visible light. New J Chem 40:3208–3215

[27] Ma J, Liu Q, Zhu L, Zou J, Wang K, Yang M, Komarneni S (2016) Visible light photocatalytic activity enhancement of Ag$_3$PO$_4$ dispersed on exfoliated bentonite for degradation of rhodamine B. Appl Catal B Environ 182:26–32

[28] Xu JW, Gao ZD, Han K, Liu Y, Song YY (2014) Synthesis of magnetically separable Ag$_3$PO$_4$/TiO$_2$/Fe$_3$O$_4$ heterostructure with enhanced photocatalytic performance under visible light for photoinactivation of bacteria. ACS Appl Mater Interfaces 6:15122–15131

[29] Li G, Mao L (2012) Magnetically separable Fe$_3$O$_4$–Ag$_3$PO$_4$ sub-micrometre composite: facile synthesis, high visible light-driven photocatalytic efficiency, and good recyclability. RSC Adv 2:5108–5111

[30] Ma J, Zou J, Li L, Yao C, Kong Y, Cui B, Zhu R, Li D (2014) Nanocomposite of attapulgite–Ag$_3$PO$_4$ for Orange II photodegradation. Appl Catal B Environ 144:36–40

[31] Yu H, Jiao Z, Hu H, Lu G, Ye J, Bi Y (2013) Fabrication of Ag$_3$PO$_4$–PAN composite nanofibers for photocatalytic applications. CrystEngComm 15:4802–4805

[32] Yu H, Dong Q, Jiao Z, Wang T, Ma J, Lu G, Bi Y (2014) Ion exchange synthesis of PAN/Ag$_3$PO$_4$ core–shell nanofibers with enhanced photocatalytic properties. J Mater Chem A 2:1668–1671

[33] Panthi G, Park S-J, Chae S-H, Kim T-W, Chung H-J, Hong S-T, Park M, Kim H-Y (2017) Immobilization of Ag$_3$PO$_4$ nanoparticles on electrospun PAN nanofibers via surface oximation: bifunctional composite membrane with enhanced photocatalytic and antimicrobial activities. J Ind Eng Chem 45:277–286

[34] Liu J, Zhou P, Zhang L, Ma Z, Liang J, Fong H (2009) Thermo-chemical reactions occurring during the oxidative stabilization of electrospun polyacrylonitrile precursor nanofibers and the resulting structural conversions. Carbon 47:1087–1095

[35] Ungár T (2004) Microstructural parameters from X-ray diffraction peak broadening. Scr Mater 51:777–781

[36] Zhao Z-P, Li J, Chen J, Chen C-X (2005) Nanofiltration membrane prepared from polyacrylonitrile ultrafiltration membrane by low-temperature plasma: 2. Grafting of styrene in vapor phase. J Membr Sci 251:239–245

[37] Gonzalez G, Albano C, Herman V, Boyer I, Monsalve A, Brito JA (2012) Nanocomposite building blocks of TiO$_2$–MWCNT$_f$ and ZrO$_2$–MWCNT$_f$. Mater Charact 64:96–106

[38] Zhu M, Chen P, Liu M (2011) Graphene oxide enwrapped Ag/AgX (X = Br, Cl) nanocomposite as a highly efficient visible-light plasmonic photocatalyst. ACS Nano 5:4529–4536

[39] Zhai W, Li G, Yu P, Yang L, Mao L (2013) Silver phosphate/carbon nanotube-stabilized pickering emulsion for highly efficient photocatalysis. J Phys Chem C 117:15183–15191

[40] Xu Y, Xu H, Yan J, Li H, Huang L, Zhang Q, Huang C, Wan H (2013) A novel visible-light-response plasmonic photocatalyst CNT/Ag/AgBr and its photocatalytic properties. Phys Chem Chem Phys 15:5821–5830